Deformation- and Damage-Free Transfer of Soft Electronics onto Highly Curved and Fragile Biological Surfaces

Kyeong Min Song[1,2,#], Myung-Kun Chung[3,#], Jeehoon Jung[4], Jungjae Park[5], Min-Uk Kim[3], Jae-Young Yoo[6], Minsu Park[7], Geumbee Lee[8], Jeehyun Hong[2], Jun-Bo Yoon[3,*], and Yeon Sik Jung [2,*]

1. Energy and Environmental Division, Korea Institute of Ceramic Engineering and Technology, 101, Soho-ro, Jinju-si, Gyeongsangnam-do, Republic of Korea, 52851
2. Department of Materials Science and Engineering, Korea Advanced Institute of Science and Technology (KAIST), 291 Daehak-ro, Yuseong-gu, Daejeon, Republic of Korea , 34141
3. School of Electrical Engineering, Korea Advanced Institute of Science and Technology (KAIST), 291 Daehak-ro, Yuseong-gu, Daejeon, Republic of Korea, 34141
4. Low Carbon Energy R&D Center, Korea Institute of Industrial Technology, 55, Jongga-ro, Jung-gu, Ulsan, Republic of Korea, 44413
5. Research Institute of Industrial Science and Technology, 156, Jungheung-ro, Buk-gu, Pohang-si, Gyeongsangbuk-do, Republic of Korea, 37673
6. Department of Semiconductor Convergence Engineering, Sungkyunkwan University (SKKU), 2066, Seobu-ro, Jangan-gu, Suwon-si, Gyeonggi-do, Republic of Korea, 31065
7. Department of Polymer Science and Engineering, Dankook University, 152, Jukjeon-ro, Suji-gu, Yongin-si, Gyeonggi-do, Republic of Korea, 16890
8. Department of Chemical Engineering, Kyungpook National University, 80, Daehak-ro, Buk-gu, Daegu, National University, Daegu, Republic of Korea, 41566.

#These authors contribute equally to this work.
*Email: jbyoon@kaist.ac.kr (J.-B.Y), ysjung@kaist.ac.kr (Y.S.J)
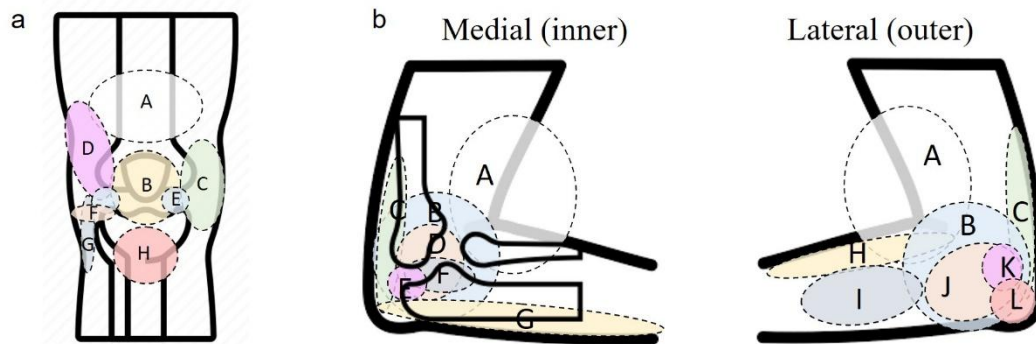
Supplementary Fig. 1 | Pain distribution map of convex joint. a, Pain diagram of knee joint**.** A Quadriceps tendonitis, B Patellofemoral pain syndrome, C MCL sprain arthritis, D ITB syndrome, E Osteochondritis dissecans, F Lateral Meniscus tear, G LCL injury, H Patellar tendonitis. **b,** Pain diagram of elbow. A Biceps tendonitis, B Hyperextended elbow, C Triceps tendonitis, D MCL sprain, E elbow apophysitis, F Golfer's elbow, G Cubital tunnel syndrome, H Brachioradialis pain, I Radial tunnel syndrome, J Tennis elbow, K Radiohumeral bursitis, L Olecranon bursitis.
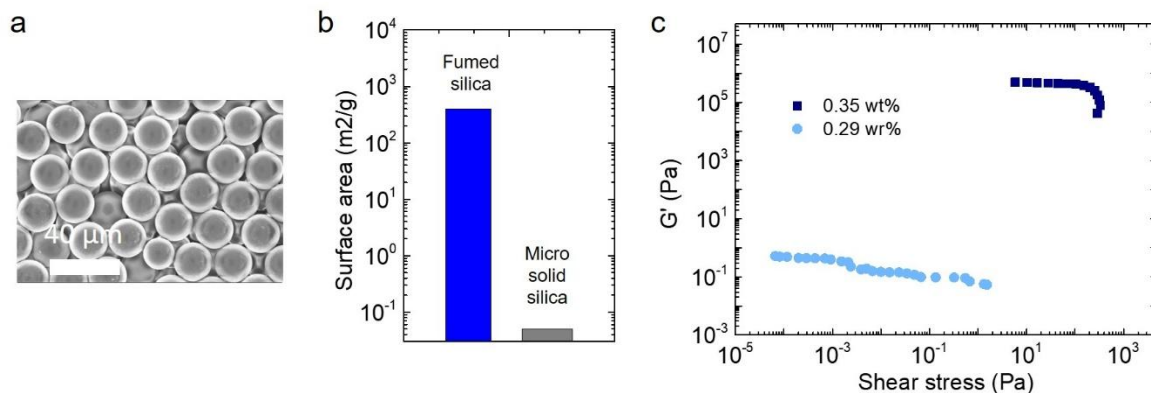

Supplementary Fig. 2 | Morphological and rheological characteristics of yield-stress fluids incorporating micro solid silica particles. a, Scanning electron microscopy (SEM) image of micro solid silica particles, showing uniform spherical morphology with a mean diameter of ~40 μm. **b,** Comparison of specific surface areas between fumed silica (used in DAYS-fluid) and micro solid silica particles, highlighting the ~$10^3\times$ higher surface area of fumed silica, which significantly contributes to yield-stress behavior through increased interparticle network formation. **c,** Storage modulus (G') of silica-based fluids as a function of solid silica concentration, demonstrating that micro solid silica requires significantly higher loading to induce comparable elastic response, indicating poor network formation capability relative to fumed silica. These results support the use of fumed silica as a more effective rheological modifier in achieving the desired yield-stress behavior for stable and decoupled transfer.

47
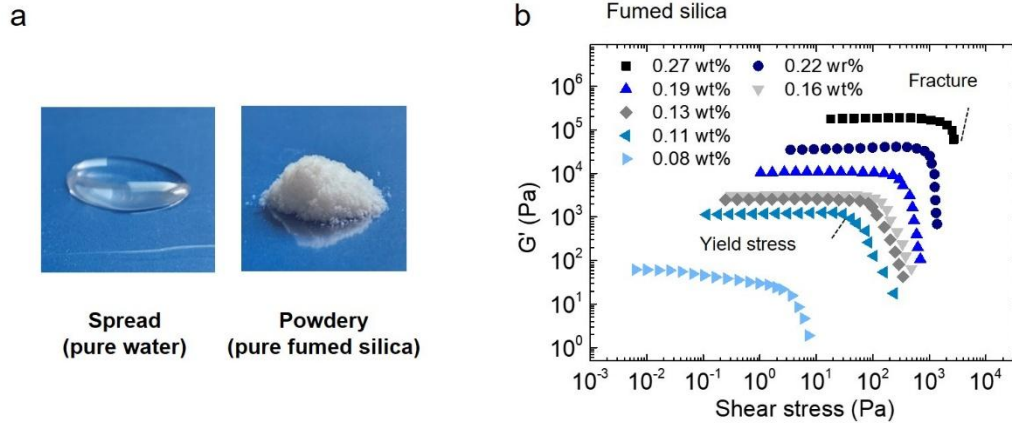
Supplementary Fig. 3 | Rheological behavior of aqueous suspensions containing fumed silica particles. a, Representative photographs of pure deionized water (left) and as-received fumed silica powder (right). g. **b,** Storage modulus (G') as a function of fumed silica concentration, showing a sharp increase in elasticity with increasing particle content. The data demonstrate that even low concentrations (~0.1–0.2 wt%) are sufficient to induce a solid-like yield-stress behavior, due to the high surface area and strong interparticle interactions of fumed silica. This tunable rheological profile underpins the design of DAYS-fluid with desired flow-deformation decoupling characteristics.

54

|	**Rupture pressure (kPa)**
Skin	1000-2000
Liver	100-500
Muscle	500-2000
Eyeball	100-360
Egg yolk	0.2-0.5

55

Supplementary Table 1 | Reported rupture pressure ranges of various biological surfaces[1-4]. This table summarizes the rupture pressures of soft biological tissues and organ analogs relevant to device transfer applications. The data highlight the extreme mechanical fragility of egg yolk (0.2–0.5 kPa), which serves as a benchmark for evaluating non-invasive transfer capability. By comparison, human skin and muscle exhibit much higher rupture thresholds (up to 2000 kPa), while internal organs such as the liver and eyeball fall within intermediate ranges. These values were used to validate that the yield stress of DAYS-fluid (~0.0024 kPa) remains safely below the mechanical failure thresholds of even the most delicate biological substrates.

63
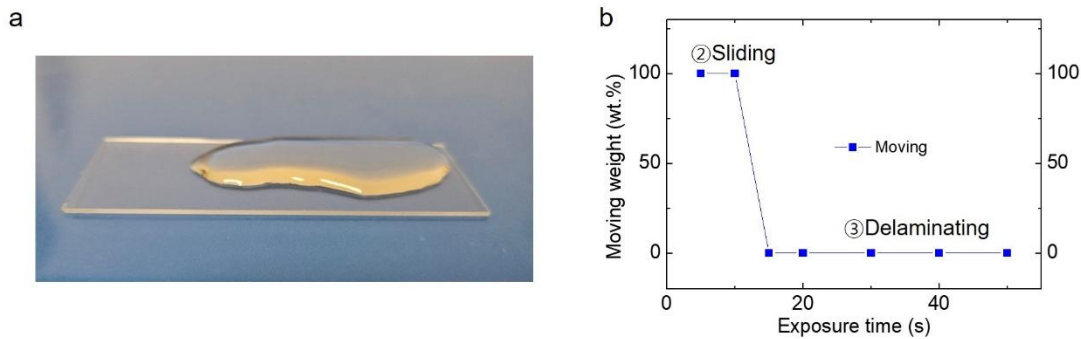
Supplementary Fig. 4 | Water-assisted mobility analysis of yield-stress fluid on wet slide glass. a, Photograph of a wet slide glass, with water uniformly applied to the surface to create a hydrated interface. This setup was used to investigate how interfacial water influences the detachment behavior of the yield-stress fluid. **b,** Graph showing the weight percentage of the moving portion of the fluid as a function of water exposure time. Sliding occurs immediately followed by near-complete detachment at longer exposure times (>15 s), indicating rapid interfacial weakening by water penetration.
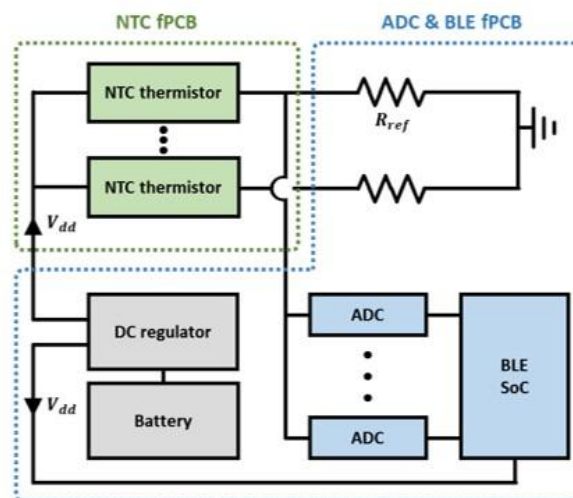

Supplementary Fig. 4 | Schematic circuit diagram of the thermal sensor array system. The system consists of two main flexible printed circuit boards (fPCBs): one for sensing (NTC fPCB) and the other for data acquisition and transmission (ADC & BLE fPCB). The NTC fPCB contains two negative temperature coefficient (NTC) thermistors that measure local skin temperature. These thermistors are connected to analog-to-digital converters (ADCs) located on the ADC & BLE fPCB, which digitize the temperature signals. A DC regulator and battery provide power to the system, while the digitized data is processed and wirelessly transmitted via a Bluetooth Low Energy system-on-chip (BLE SoC). This modular design allows for compact integration and real-time wireless temperature monitoring on soft or curved biological surfaces.

82
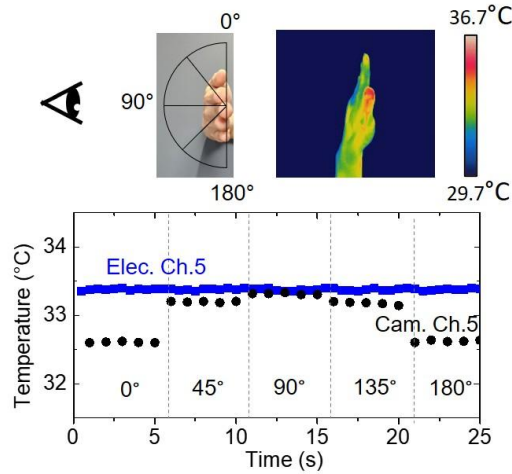
Supplementary Fig. 6 | Real-time thermal sensing of finger joints under varying postures. (Top) Photographic image (left) and corresponding IR thermography (right) show the hand positioned across five angular postures. Temperature data recorded by the DAYS-fluid-transferred thermal sensor array (blue trace) and by an IR camera (black trace) across different angles. The thermal sensor array maintains stable output with deviations within ±0.014 °C across all postures, while the IR camera exhibits significant fluctuations due to inconsistent surface targeting. This demonstrates the superior conformality and measurement stability of our system on dynamically moving anatomical regions.

90

91
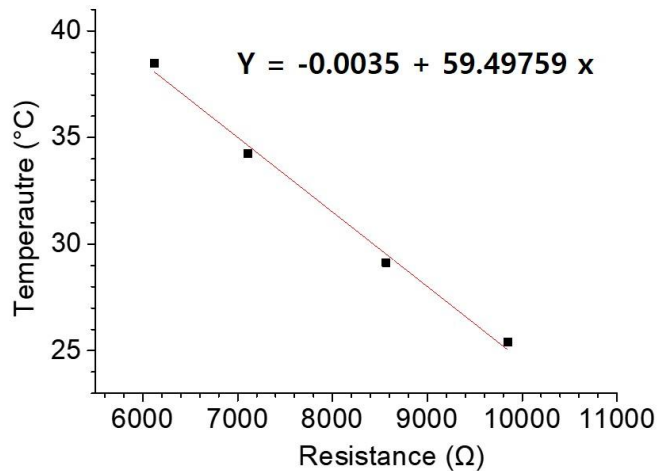
Supplementary Fig. 7 | Calibration curve of the thermal sensor array. Linear correlation between resistance (Ω) and temperature (°C) measured using the NTC thermistor-based sensor array. The calibration data were fitted with a linear regression (red line), showing high accuracy ($R^2 \approx 0.999$) across the physiological temperature range (25–45 °C), enabling precise skin temperature quantification during real-time monitoring.

96
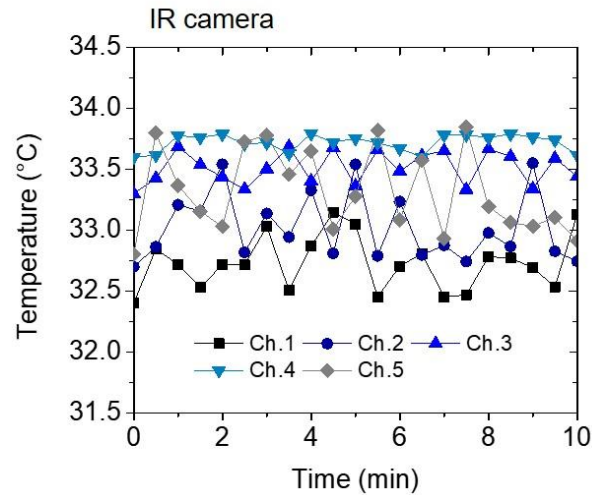
Supplementary Fig. 8 | Inconsistent temperature readings from IR camera during finger typing. Temperature variations at the index finger joint were recorded during repeated typing using an IR camera. The plot shows large fluctuations and noise across different frames, with deviations frequently exceeding ±0.5 °C. These inconsistencies are attributed to posture-dependent detection zones and limited spatial resolution of IR thermography, highlighting the need for conforml and contact-based thermal sensors for accurate monitoring.
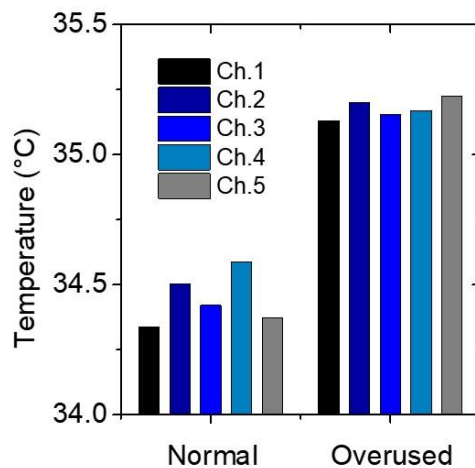
Supplementary Fig. 9 | Temperature comparison between normal and overused fingers measured by thermal sensor array. The bar graph shows the temperature values from each sensing channel (Ch.1 to Ch.5) placed on the left hand. To induce overuse, the subject repeatedly clenched and unclenched the hand more than 20 times prior to measurement. All five channels exhibited a clear temperature elevation in the overused condition, with increases of approximately 0.6–0.85 °C compared to the normal condition, indicating reliable detection of localized inflammation-related thermal signals.

Supplementary references

1. Eschenhagen, D. R. On the resistance of tissues to distortion. *J. Anat. Physiol.* **57**, 318–319 (1898).

2. Swayne, D. E., Glisson, J. R., McDougald, L. R., Nolan, L. K., Suarez, D. L. & Nair, V. L. *Diseases of Poultry*. Wiley-Blackwell (2013). ISBN: 9781119371168.

3. Welch, A. J. & Gemert, M. J. C. *Optical-Thermal Response of Laser-Irradiated Tissue*. Physics in Medicine & Biology (2011). ISBN: 978-90-481-8830-7.

4. Hukki, J. et al. A case study of amnion rupture sequence with acalvaria, blindness, and clefting. *J. Craniofac. Surg.* **15**, 185–191 (2004).